Annual Report

Kinetic Isolation Tether Experiment

(Grant No. NCC 2-389)

submitted to

NASA Ames Research Center

Moffett Field, CA 94033

by

Guidance and Control Laboratory
Aeronautics and Astronautics Dept.
Stanford University
Stanford, CA 94305

J. David Powell, Principal Investigator
Xiaohua He, Research Assistant
Robert Schoder, Research Assistant

February 1988

1 Executive Summary

Progress has been made during the past year on the analysis of tether damping and on experimentation of the control system on the laboratory simulator.

The damping analysis considers the dynamics of a long tether connecting two spacecraft in Earth orbit, one of the spacecraft having dominant mass. In particular, it considers the material damping of the tether. The nominal position of the tether is stabilized by the gravity gradient such that it is aligned with the local vertical. The tether is modeled as an visco-elastic flexible continuum. Modal frequencies are derived in an analytical approximation form. Damping ratios are estimated according to the linear model calibrated by ground measurements. The results show that, with properly chosen tether material and braiding structure, longitudinal vibration of the tethered system is well damped. The damping ratio of the mass-spring mode depends not only on tether material damping property but also on tether mass to satellite mass ratio and tether length. All of the high-frequency vibration modes typically have a damping ratio in excess of 0.15 which is determined by tether material damping property only. Lateral string vibration of a long tether has an extremely small damping ratio which is proportional to the square of the amplitude. The jump-rope mode has no damping in its pure rotation. However, it will precess into the damped planar vibration over several orbits.

A particularly effective method of implementing attitude control for tethered satellites is to use the tether tension force to generate control torques by moving the tether attach point relative to the satellite center of mass. A scaled, one dimensional laboratory simulation of the KITE mission has been built and preliminary experiments of the proposed attitude control system were performed. The simulator was built to verify theoretical predictions of attitude control ability and to investigate the technological requirements in order to implement this concept. A detailed description of the laboratory apparatus follows and, in addition, the results of the preliminary experiments are presented and discussed. The results to date have shown a fine pointing accuracy of 5 arc-seconds RMS and a closed-loop bandwidth of .08 Hz.

2 The Analysis of Tether Damping

2.1 Introduction

Tether applications in space were proposed in the 1960s, though the idea can be traced back to the end of the last century. In recent years, thanks to the development of space and material technology, the concept has become a viable new option in various scientific experiments and engineering applications. The first tests of tethered spacecraft were conducted on the Gemini XI and XII missions. Since then, many applications have been proposed, such as tethered micro-gravity experiments, tether electric power generation, tether momentum transfer, tether propulsion, and tether isolation for instrument mounts.

The dynamic analyses and simulation of tethers using various methods and models have been ongoing for years. However, the damping properties of tethers have not been treated thoroughly. No method has been reported for using ground measurements to predict tethered system damping in flight configurations. Damping ratios of the spring-mass mode of scaled down models in ground tests have been reported [1]; however, these data are for significantly different lengths and end masses than the space applications. For most applications, tether damping is important to keep the tethered system stable and to have a quiet environment. Although damping can be supplied by active means (*e.g.* TSS [2]), it is more desirable to provide an adequate amount of passive damping. In the Kinetic Isolation Tether Experiment (KITE) [3], the tether damping property directly affects the disturbance propagation along the tether and thus determines the effectiveness of its isolation. Therefore, a method to estimate the damping of tethers and the damping of tethered systems in space need to be derived.

Moreover, there is a jump-rope (or "skip-rope") mode which apparently has not been thoroughly studied, though it was observed in an orbit flight experiment twenty years ago on Gemini XI [4]. Since there is no elongation variation involved in this mode, there is no damping in the mode. Lack of damping could cause trouble in some applications. Therefore, the jump-rope mode requires careful study.

The tethered satellite systems studied in this paper consist of two spacecraft connected by a long flexible tether. One of the spacecraft, the parent,

has the dominant mass of the system. The system is stabilized in orbit by the gravity gradient which aligns the tether with the local vertical in its nominal position. The mass of the tether is substantially smaller than that of the spacecraft at either end, and the tether can be modeled as a uniform continuum without bending resistance. Assuming small perturbations, the dynamics of a tethered system are considered separately as pendular libration, steady elongation, longitudinal vibration and lateral vibration. The partial differential equations of motion are solved using the Laplace transform; that is, in the complex frequency domain, since natural frequencies and damping ratios are of primary interest. To have a better understanding of the relations between various parameters and to avoid long computation time, solutions are given in an approximate analytical form.

The longitudinal vibration problem is solved neglecting the coupling from lateral vibration which would result from the orbital motion. Two different damping models, structural and viscous, are applied and combined. The solution leads to a method to estimate the damping property of tethered satellite systems in space. The lateral vibration problem is solved considering the longitudinal coupling effect which slightly shifts the natural frequencies of in-plane lateral vibration. The damping effect in lateral vibration due to the associated elongation rate is estimated from the point of view of energy dissipation. The jump-rope mode is discussed as a special case of the superposition of two lateral vibration modes in two orthogonal planes, 90° out of phase. There is no material damping associated with the jump-rope mode, since no change in elongation occurs. However, the orbit coupling makes the jump-rope rotation alternate periodically with planar vibration that is damped.

Theoretical analysis is presented in the next section. An example of damping ratio estimation based on ground tests is given in Section 2.3.

2.2 Mathematical Models and Analysis

The analysis in this paper is based on the following assumptions :

- Both of the spacecraft are point masses.
- The parent spacecraft is orbiting in an unperturbed circular orbit.

- The nominal position of the tether is aligned with the local vertical.
- Deviations from the nominal position are small compared to tether length.
- The tether is perfectly flexible *i.e.*, has no bending resistance.
- The tether is linear elastic with material damping.

The coordinate system used originates in the unperturbed circular orbit of the parent spacecraft. The roll-axis X is in the orbital velocity direction, the yaw-axis Z is pointing down along the local vertical, and the pitch axis Y is then defined by the right-hand rule, as is shown in Figure 1.

According to Euler-Hill's equation [5] and linear elasticity [6], the equations of motion of the tether can be written as

$$\rho A\left(\frac{\partial^2 x}{\partial t^2}-2n\frac{\partial u}{\partial t}\right)=\frac{\partial}{\partial z}\left(T\frac{\partial x}{\partial z}\right) \tag{1}$$

$$\rho A\left(\frac{\partial^2 u}{\partial t^2}+2n\frac{\partial x}{\partial t}-3n^2u\right)=3n^2z\rho A+\frac{\partial T}{\partial z}+f \tag{2}$$

$$\rho A\left(\frac{\partial^2 y}{\partial t^2}+n^2y\right)=\frac{\partial}{\partial z}\left(T\frac{\partial y}{\partial z}\right) \tag{3}$$

$$T=EA\frac{\partial u}{\partial z} \tag{4}$$

where $x=x(z,t)$, $y=y(z,t)$ and $u=u(z,t)$ are the perturbation of the point $(0,0,z)$ in X, Y and Z directions, respectively. T is the tension force in the tether, and f is the material damping force per unit length.

$E \equiv$ Young's modulus; $\rho \equiv$ Tether density;
$A \equiv$ Tether cross section area; $n \equiv$ Orbit rate.

For such a space system, the frequencies of structural vibration modes (> 0.01 rad/sec) are much higher than those of orbital motion determined modes, known as in-plane and out-of-plane pendular libration modes having natural frequencies of $\sqrt{3}n$ and $2n$ ($n \cong 0.001$ rad/sec), respectively. That is, the structural vibration is decoupled from libration modes. Therefore, the libration modes are ignored in the following structural vibration

analyses, though they can be analyzed separately using a rigid tether model and then superimposed.

By virtue of the small tether mass to satellite mass ratio, the lateral displacement at the satellite end of the tether is approximately zero [7]. As a result, the boundary conditions for the dynamic equations of the tether can be expressed as

$$x(0,t) = y(0,t) = u(0,t) = 0, \tag{5}$$

$$x(L,t) \cong y(L,t) \cong 0 \tag{6}$$

$$EA\frac{\partial u}{\partial z}(L,t) = T(L,t). \tag{7}$$

Considering the dynamics of the satellite, tether tension at the end is related to the acceleration of the satellite as

$$T(L,t) = 3n^2LM - M\frac{\partial^2 u}{\partial t^2}(L,t), \tag{8}$$

where M representing satellite mass and L representing tether length.

Due to linearity, longitudinal displacement can be split into two parts as

$$u = u_1 + u_2. \tag{9}$$

u_1 is the time independent solution which represents the steady stretch due to the gravity gradient. u_2 is the time varying deviation of the tether displacement from u_1.

Neglecting all the time derivative terms in Equation (2), (4) and the boundary conditions on $u(z,t)$, a set of time independent equations and boundary conditions for u_1 are found as

$$C_0^2\frac{\partial^2 u_1}{\partial z^2} + 3n^2u_1 + 3n^2z = 0. \tag{10}$$

$$u_1(0,t) = 0, \tag{11}$$

$$\frac{\partial u_1}{\partial z}(L,t) = 3n^2ML/(EA); \tag{12}$$

where $C_0 \equiv \sqrt{\frac{EA}{\rho A}}$ is the speed of sound in the tether. This equation can be solved independently. The solution given in Equation (13) is the steady elongation of the tether due to the gravity gradient.

$$u_1(z) = K_1 \sin\left(\frac{\sqrt{3}n}{C_0} z\right) - z, \tag{13}$$

where

$$K_1 = \frac{1 + 3n^2 LM/(EA)}{\frac{\sqrt{3}n}{C_0} \cos\left(\frac{\sqrt{3}n}{C_0} L\right)}. \tag{14}$$

Knowing that the orbit rate is substantially lower than those of structural vibrations [8] considered here, the coupling term from in-plane lateral motion to longitudinal motion through orbit rotation can be ignored in Equation (2). Subtracting u_1 from Equation (2), (4), and the corresponding boundary conditions given in Equation (5) and (7), the equation of longitudinal motion becomes

$$\frac{\partial^2 u_2}{\partial t^2} - 3n^2 u_2 - C_0^2 \frac{\partial^2 u_2}{\partial z^2} - f/(\rho A) = 0, \tag{15}$$

$$u_2(0,t) = 0, \tag{16}$$

$$\frac{\partial u_2}{\partial z}(L,t) = \frac{1}{EA} T(L,t). \tag{17}$$

2.2.1 Longitudinal Dynamics

As is derived previously, the longitudinal dynamics of the tethered system is described by Equation (15), (16) and (17). The mode shapes expected are illustrated in Figure 2.

According to the theory of elasticity, there are two commonly used models to describe material damping *i.e.*, structural damping and viscous damping. Both can be expressed as

$$f = bEA \frac{\partial^2}{\partial z^2}\left(\frac{\partial u_2}{\partial t}\right). \tag{18}$$

In the case of viscous damping, b is a constant damping coefficient. In the case of structural damping, b $(= \gamma/\omega)$ depends on the driving frequency ω, where γ is a constant, structural damping coefficient [6].

Since the natural frequencies and damping ratios of various modes are of primary interest, the Laplace transform is applied. Equation (15), (16) and (17) become

$$\frac{\partial^2 U_2(z,s)}{\partial z^2} - \frac{s^2 - 3n^2}{(C_0/L)^2(1+bs)} U_2(z,s) = 0, \tag{19}$$

$$U_2(0,s) = 0, \tag{20}$$

$$\frac{\partial U_2}{\partial z}(L,s) = \frac{1}{EA} T(L,s). \tag{21}$$

The solution in terms of the unknown tether tension at the satellite attachment point is :

$$U_2(z,s) = \left(\frac{L}{EA}\right) \frac{\sin(\lambda z)/(\lambda L)}{\cos(\lambda L)} T(L,s), \tag{22}$$

where

$$\lambda^2 \equiv \frac{-(s^2 - 3n^2)}{(C_0/L)^2(1+bs)}. \tag{23}$$

Writing the sinusoidal functions in Equation (22) in the factored form [9], the tension force at the satellite end of the tether can be expressed, using a transfer function, in terms of the displacement at the same end :

$$T(L,s) = KG(s)\, U_2(L,s) \tag{24}$$

where

$$G(s) = \prod_{k=1}^{\infty} \left\{ \left(\frac{2k}{2k-1}\right)^2 \frac{\left[s^2 + b(2k-1)^2\left(\frac{\pi C_0}{2L}\right)s + (2k-1)^2\left(\frac{\pi C_0}{2L}\right)^2 - 3n^2\right]}{\left[s^2 + b(2k)^2\left(\frac{\pi C_0}{2L}\right)s + (2k)^2\left(\frac{\pi C_0}{2L}\right)^2 - 3n^2\right]} \right\}, \tag{25}$$

and

$$K \equiv EA/L. \tag{26}$$

In the case of structural damping, Equation (25) is not a conventional transfer function because some of the coefficients depend on input frequency. However, when $\gamma^{1.5} \ll 2$, frequency response will not be changed

substantially if γ/ω is replaced by γ/ω_k in each second order factor of the formal transfer function of Equation (25), where

$$\omega_k = k\omega_0\sqrt{1-3\left(\frac{n}{k\omega_0}\right)^2} \tag{27}$$

and

$$\omega_0 \equiv \frac{\pi C_0}{2L}. \tag{28}$$

For a second order factor, the relative error of frequency response due to the above substitution is bounded below $\gamma^{1.5}/2$.

This substitution makes Equation (25) a conventional transfer function. Therefore, the transfer function in both cases can be written as

$$G(s) = \prod_{k=1}^{\infty}\left[\left(\omega_{2k}/\omega_{2k-1}\right)^2 \frac{\left(s^2+2\xi_{2k-1}\omega_{2k-1}+\omega_{2k-1}^2\right)}{\left(s^2+2\xi_{2k}\omega_{2k}+\omega_{2k}^2\right)}\right], \tag{29}$$

where in the case of viscous damping

$$\xi_i = i\xi_v/\sqrt{1-3\left(\frac{n}{k\omega_0}\right)^2}, \tag{30}$$

$$\xi_v = \frac{b\omega_0}{2} = \frac{\pi b C_0}{4L}; \tag{31}$$

and in the case of structural damping

$$\xi_i = \xi_s/\sqrt{1-3\left(\frac{n}{k\omega_0}\right)^2}, \tag{32}$$

$$\xi_s = \frac{\gamma}{2}. \tag{33}$$

Figure 3 shows the pole-zero locations of the tether transfer function on a complex frequency plane for both cases. Obviously, the structural damping model results in less damped high-frequency modes compared to the viscous damping model, provided the first modes have the same damping ratio. In other words, a safer, relatively more conservative damping estimate on high-frequency structural vibration is expected from the structural damping model when no adequate data on damping ratios of the higher order modes is available to determine which model is more accurate.

Considering the dynamics of the satellite mass, the displacement at the end of the tether can be written as:

$$U_2(L,s) = -\frac{1}{Ms^2}T(L,s). \tag{34}$$

The longitudinal dynamics of the tethered satellite system can be expressed in block-diagram form, as shown in Figure 4. The characteristic equation for the combined system (the tether and end mass) is:

$$1 + \left(\frac{K}{M}\right)\frac{G(s)}{s^2} = 0. \tag{35}$$

For low-frequency dynamics, the characteristic equation is solved under the assumption that $s \ll \omega_0$. Through some algebra and approximation, the two lowest frequency characteristic roots of the combined system are found as

$$s_m \cong -\xi_m\omega_m \pm j\omega_m\sqrt{1-\xi_m^2}, \tag{36}$$

with

$$\omega_m = \sqrt{\frac{K}{M}} = \frac{2}{\pi}\sqrt{\eta}\omega_0 \tag{37}$$

that yields

$$\frac{\omega_m}{\omega_0} = (2/\pi)\sqrt{\eta}, \tag{38}$$

and

$$\xi_m = \xi_0\left(\frac{\omega_m}{\omega_0}\right) = \frac{2}{\pi}\sqrt{\eta}\xi_0, \tag{39}$$

where

$$\eta \equiv \frac{m}{M} = \frac{\rho AL}{M} \tag{40}$$

and $m \equiv$ tether mass.

This low-frequency dynamic mode is called the mass-spring mode, since ω_m $(= \sqrt{K/M})$ is simply the natural frequency of a mass-spring system, where the equivalent spring constant is $K = EA/L$.

ξ_0 could be either ξ_v or ξs, or the sum of the two. In general,

$$\xi_m = \left(\frac{\omega_m}{\omega_0}\right)(\xi_s + \xi_v) = a_1\sqrt{\frac{L}{M}} + a_2\frac{1}{\sqrt{ML}}, \tag{41}$$

where

$$a_1 \equiv \frac{\gamma}{\pi}\sqrt{\rho A}, \tag{42}$$

$$a_2 \equiv \frac{b}{2}\sqrt{EA}. \tag{43}$$

The effect of the end mass (satellite) essentially affects only low-frequency dynamics of the tether, if the tether/satellite mass ratio is small ($\eta < 1$), which will typically be the case. In the high-frequency region, the characteristic roots in Figure 3 are hardly moved as the result of the end mass effect. They are approximately

$$s_k = -\xi_{2k}\omega_{2k} \pm \omega_{2k}\sqrt{1-\xi_{2k}^2}, \tag{44}$$

which indicates that the natural frequency and damping ratio of the kth structural vibration mode of the tethered system are approximately ω_{2k} and ξ_{2k}.

Note that these poles are exactly those of a tether with both ends fixed, the case of infinite end mass. The deviation of poles due to the effect of finite end mass is proved to be less than $(\eta/k\pi^2)\omega_0$ for the kth mode. The relative error in norm is bounded by $\eta/(k\pi)^2$ that is less than 10 % for most of the potential space applications. For instance, the relative error is less than 0.2 % for KITE configuration and 3 % for the TSS-1.

The zeros of the tether/end mass combined system, shown in Figure 4, are exactly those poles of the tether transfer function, the poles of the tether with infinite end mass. Therefore, the poles of the combined system are close to the zeros of the same system. In other words, the system zeros tend to cancel the system poles except the first low-frequency pair that are associated with the mass-spring mode. The pole-zero "cancellation" indicates that the structural vibration modes given in Equation (44) are almost unobservable through the end mass displacement. Physically, this can be interpreted that the end point is very close to one of the node points in all the structural vibration modes, due to the small tether mass to end mass ratio, $\eta < 1$.

2.2.2 Lateral Dynamics

Lateral dynamics are described in Equation (3), and Equation (1) coupled with (15). The boundary conditions are given in Equations (5) and (6).

Assuming small perturbation, $|u_2| \ll |u_1|$, and according to Equations (9) , (4) and (13), the tension force can be written as

$$T \cong EA\frac{\partial u_1}{\partial z} = EA\left[\left(1+\frac{3n^2}{\omega_m^2}\right)\frac{\cos(\sqrt{3}nz/C_0)}{\cos(\sqrt{3}nL/C_0)} - 1\right]. \tag{45}$$

Considering that $nz/C_0 < nL/C_0 \ll 1$, the tension can be represented by its average value along the tether :

$$T \cong EA\left[\left(\frac{\sqrt{3}n}{\omega_m}\right)^2 + \left(\frac{nL}{C_0}\right)^2\right]. \tag{46}$$

With the above approximation, the lateral dynamic equations can be written as

$$\frac{\partial^2 y}{\partial t^2} + n^2 y - (\alpha C_0)^2\frac{\partial^2 y}{\partial z^2} = 0, \tag{47}$$

$$\frac{\partial^2 x}{\partial t^2} - (\alpha C_0)^2\frac{\partial^2 x}{\partial z^2} - 2n\frac{\partial u_2}{\partial t} = 0, \tag{48}$$

$$\frac{\partial^2 u_2}{\partial t^2} - 3n^2 u_2 + 2n\frac{\partial x}{\partial t} = C_0^2\frac{\partial^2 u_2}{\partial z^2} + f/\rho A, \tag{49}$$

where

$$\alpha \equiv \frac{\sqrt{3}n}{\omega_m}\sqrt{1+\eta/3}. \tag{50}$$

The natural frequencies of lateral vibration in both planes can be found by solving the eigenvalue problem of the above equations. The solution is

$$\omega_{xk} \cong k\omega_1\sqrt{1-\left(\frac{2\alpha n}{k\omega_1}\right)^2} \tag{51}$$

for kth lateral vibration mode in X-Z plane, and

$$\omega_{yk} \cong k\omega_1\sqrt{1+\left(\frac{n}{k\omega_1}\right)^2} \tag{52}$$

for kth lateral vibration mode in Y-Z plane, where

$$\omega_1 \equiv 2\alpha\omega_0 = \frac{\pi\sqrt{3}n}{\sqrt{\eta}}\sqrt{1+\eta/3}. \tag{53}$$

Clearly, these frequencies are much lower than those of longitudinal structural vibration modes, since $\alpha \ll 1$ for most potential tethered systems in space. Furthermore, it also appears that ω_1 will be substantially greater than orbit rate in most cases. For the 20 km TSS-1, ω_1 is 0.01 rad/sec, and for the 2 km KITE tethered satellite, ω_1 is 0.1 rad/sec, both of which are much fast than the typical orbit rate of 0.001 rad/sec. The frequency separation assumed previously is assured.

Modal frequencies in the two orthogonal planes are very close and approximately equal to $k\omega_1$. This approximate result can be obtained from the lateral dynamic equations neglecting the cross coupling due to orbit rotation, as has been done by Suchet [10]. The difference between the modal frequencies in the two planes is introduced by cross coupling from longitudinal motion to in-plane lateral motion and can be found by subtracting Equation (51) from Equation (52) *i.e.*,

$$\Delta\omega_k \equiv \omega_{yk} - \omega_{xk} \cong \frac{1}{2}\left(\frac{n}{k\omega_1}\right) n = \frac{n/k}{2\sqrt{3}\pi}\sqrt{\eta}/\sqrt{1+\eta/3}. \qquad (54)$$

Since no bending resistance is considered, there is no damping in lateral vibration modes. The damping of lateral motion relies on the non-linear coupling between lateral motion and longitudinal motion. Instead of considering this non-linear coupling, the damping effect in lateral motion can be estimated from the energy point of view. If we consider the elongation engaged in the lateral deformation, an elongation rate and, thus, energy dissipation exists via the damping properties of the longitudinal motion. Since the modal frequencies of in-plane, X-Z, and out-of-plane, Y-Z, lateral vibration are fairly close, the following discussion of the damping property of lateral vibration applies to both cases, with modal frequencies approximated as

$$\omega_{xk} \cong \omega_{ky} \cong k\omega_1. \qquad (55)$$

It is reasonable to assume that the longitudinal strain engaged in lateral deformation is uniformly distributed along the tether. Then the maximum tether elongation engaged in the kth lateral vibration mode can be expressed approximately as

$$\Delta L \cong k\,(\pi/2)^2\,(B_k/L)\,B_k, \qquad (56)$$

provided the ratio of lateral vibration amplitude B_k to tether length L is small, $(B_k/L) \ll 1$.

The uniform stretch due to lateral vibration essentially excites only the mass-spring mode. The energy dissipated in each cycle of the forced vibration can be expressed as [6]

$$\Delta E_l = C_l \pi \omega (\Delta L)^2 \tag{57}$$

where $C_l \equiv 2\xi_m \omega_m M$, and the driving frequency is the lateral vibration modal frequency, $\omega = k\omega_1 = 2k\alpha\omega_0$. On the other hand, the energy dissipated in each cycle of the kth lateral vibration mode can be written equivalently as

$$\Delta E_k = C_k \pi \omega B_k^2. \tag{58}$$

Since the energy dissipated in lateral vibration is entirely due to the associated elongation rate, the energy loss given in the above two equations should be the same *i.e.*,

$$\Delta E_l = \Delta E_k. \tag{59}$$

Accordingly, with the equivalent damping coefficient defined by

$$C_k \equiv \xi_k \left(k\omega_1\right) \left(\rho A L\right), \tag{60}$$

the damping ratio of the kth lateral vibration mode is

$$\xi_k = \left(\frac{k}{\alpha}\right) \left(\frac{\pi}{2}\right)^2 (B_k/L)^2 \, \xi_0. \tag{61}$$

The damping ratio is not, as is usually the case, a constant because the damping in lateral motion is introduced by the longitudinal elongation rate through non-linear coupling. Since the damping ratio is inversely proportional to $\alpha = (\sqrt{3}n/\omega_m)\sqrt{1+\eta/3}$, a higher spring-constant tether and lower satellite mass lend the system a higher lateral damping ratio. Obviously, the lateral vibration is poorly damped for small amplitudes even if the longitudinal vibration of the tether is critically damped. Additional, possibly active, damping devices may be required for the applications demanding low dynamic noise and high stability.

2.2.3 Jump-Rope Mode

The jump-rope mode is a rigid-body revolution of the tether between its two ends. Basically, it consists of the lateral mode shapes rotating about an axis along the nominal tether position, similar to the motion of a rope when a person is playing "jump-rope" or "skip-rope." Although a constant elongation exists during the motion, there is no elongation change and thus no material damping occurs. Therefore, pure jump-rope modes are not naturally damped. The first jump-rope mode was actually observed in space during the Gemini XI mission. It was excited near the termination of tether deployment and subsided later due to tether slack [4] . The jump-rope mode can be explained by prior lateral motion analysis in this paper. It is actually a special case involving the superposition of the in-plane and out-of-plane lateral vibration modes. In this special case, vibrations in both planes have the same frequency and amplitude, but differ in phase by 90 degrees.

According to the prior analysis, for the case of a tether in orbit, the frequencies of lateral vibration modes in two planes are different by $\Delta\omega_k$ for the kth mode, as is given in Equation (54). This frequency difference kills a pure jump-rope rotation by changing the phase difference of the vibration modes in two orthogonal planes. An exchange occurs between jump-rope rotation and planar lateral vibration thus producing a beat phenomenon. As discussed earlier, planar lateral motion introduces an elongation rate and material damping. The beat frequency is the frequency difference given in Equation (54). In each cycle of the beat, the mode of motion alternates twice between pure rotation and planar vibration. Figure 5 illustrates the end view of mode shapes of the beating jump-rope motion in different moments. For the kth mode, the beat time period is

$$\tau_k = 2\left(\frac{k\omega_1}{n}\right)P = 2\pi k\sqrt{3/\eta + 1}P \qquad (62)$$

where $P \equiv$ orbit period.

Intuitively, the lowest energy mode, the first mode, is the one most easily excited. Equation (62) shows that it has the shortest beat period. In other words, it will first become a pure planar vibration in $\tau_1/4$ (5 orbit periods for the case of a 20 km TSS-1 tether and 22 orbit periods for the

case of a 2 km TSS-1 tether) after being excited, and will come back to pure jump-rope rotation in another $\tau_1/4$ with decreased amplitude. The beating jump-rope mode is poorly damped, since lateral planar vibration, where the damping originates, is also poorly damped. The equivalent damping ratio of the beating mode is about half of that of the corresponding planar lateral vibration mode.

2.3 Damping Ratio and Test Data

Some experimental measurements of a tether fabricated for the TSS-1 mission have been provided by Martin Marietta Denver Aerospace, Inc. [1]. The experiment was performed in a warehouse-like ambient condition. A tether sample of various lengths was hanged with a load of various mass at the bottom end. After longitudinal oscillation was started by a well-controlled initial condition that excites only the mass-spring oscillation mode, the natural frequency (ω_n) was calculated from the output of an accelerometer mounted on the load mass. The damping ratio was also calculated from the output of the accelerometer according to a second-order system model in which the displacement of the load mass is given by

$$y(t) = Y_0 \exp(-\xi\omega_n t)\cos(\omega_n t + \phi). \tag{63}$$

Considering the ground atmosphere ambient condition, there could be some damping due to air-friction on the tether skin and aerodynamic drag on the load mass. Fortunately, the air-drag effect on the measured damping ratio was calculated to be less than one percent according to aerodynamic analysis.

For the configuration of the experiment described, prior analysis in this paper is applicable with the orbit rate n set to zero. Accordingly, the observed oscillation is the mass-spring mode with the natural frequency given in Equation (37). The damping ratio is contributed by both the structural and the viscous damping discussed previously in this paper and is given in Equation (41).

Using least squares estimation, the structural and viscous damping coefficients of the TSS-1 tether material are determined as

$$\gamma = 0.29,$$

$$b = 5.4 \times 10^{-4}\,(sec)\,.$$

In the least squares estimation, measured data with too small mass (0.226 kg) are excluded due to their large tether to load mass ratio which introduced a large error in the approximate model. Stiffness parameters are determined by measured frequencies as

$$EA = 5.29 \times 10^{4}\,(N)$$

Together with the tether density [11] given as

$$\rho A = 8.2\,(kg/km)\,,$$

Equation (41) is determined to be

$$\xi_m \cong 0.0083\sqrt{\frac{L}{M}} + 0.062\frac{1}{\sqrt{ML}} \tag{64}$$

with L in meters and M in kilograms.

Dividing the viscous damping component by the total damping ratio, the portion of viscous damping is

$$\nu \equiv \frac{\xi_{mv}}{\xi_m} = \frac{1}{1 + 0.133L}. \tag{65}$$

For the ground tests with short tethers (4 to 18 m), the viscous damping accounts for 65 % to 29 % of the total damping. On the other hand, the viscous damping contributes less than 1 % for a tethered satellite system in space with long tether (> 1 km). Therefore, viscous damping is negligible in space configurations *i.e.*,

$$\xi_m \cong 0.0083\sqrt{L/M}, \tag{66}$$

or in a dimensionless form

$$\xi_m \cong \frac{\gamma}{\pi}\sqrt{\eta} = 0.092\sqrt{\eta} \tag{67}$$

which means that the damping ratio of the mass-spring mode is determined by tether material damping and tether/load mass ratio. Using this TSS-1 tether in a tethered satellite system, with a length of 20 km and satellite

mass of 500 kg, the damping ratio of the mass-spring mode is approximately 5.5 %. On the other hand, the same tether material used on a 2 km tether with a 1000 kg satellite would yield a damping ratio of 1.2 %.

For higher frequency modes, according to Equations (31) and (33), the damping ratios are

$$\xi_{2k} = \gamma/2 + b\omega_0/2 \cong 0.15 + 1.1k/L. \tag{68}$$

Again, structural damping is dominant, which means that the damping ratio of high-frequency structural vibration modes is virtually a constant, independent of tether length and satellite mass, 0.15 in this case.

The prior discussion indicates that the longitudinal high-frequency vibration modes of a tethered satellite system are well damped, although the low-frequency mass-spring mode is not well damped for the case of light (small η) tether. The lateral vibration and the jump-rope mode are poorly damped. For a 2 km long TSS-1 tether, it takes 6 hours for the normalized amplitude (B/L) to decay from 5 % to 1 % and half month to decay from 1 % to 0.1 %. For a 100 km long TSS-1 tether, it takes 12 days for the amplitude to decay from 5 % to 1 % and two years from 1 % to 0.1 %. For the case of the jump-rope mode, the decay time is about twice of that for the planar vibration.

The material damping coefficient determined here are about two orders of magnitude higher than those of Kevlar/Epoxy beams measured in a vacuum chamber by Donald Edberg [12]. This leads to the speculation that much of the damping in the TSS-1 tether is due to the braiding and multilayer structure of the tether instead of internal damping of the material. If a tether of substantially different structure was fabricated, its damping properties could be substantially less.

It is interesting to look at the damping time constant which is defined as

$$\tau_D \equiv \frac{1}{\xi\omega}. \tag{69}$$

For the TSS-1 tether, the damping time constant of the mass-spring longitudinal mode is determined by load mass only *i.e.*,

$$\tau_{Dm} = \frac{1}{(a_1 + a_2/L)} \frac{M}{\sqrt{EA}} \cong 0.54M\,(sec)\,, \tag{70}$$

with M in kilograms; and that of kth higher frequency structural vibration modes are determined by tether length only *i.e.*,

$$\tau_{Dk} = \frac{1}{\xi_{2k}\omega_{2k}} \cong \frac{0.45}{k} L\,(sec) \tag{71}$$

with L in kilometers. The time constants are plotted in Figures 6 and 7, versus load mass and tether length, respectively. Note that damping time would only be a factor for the mass-spring mode, since decay times of structural vibration modes are typically only a few seconds.

2.4 Tether Damping Conclusions

The linear model of structural damping combined with viscous damping closely reproduce the material damping properties of tethers made of braided Kevlar fibers. The component of viscous damping is negligible for the systems having a long tether but might be significant for the system having a short (< 30 m) tether. Therefore, the effect of viscous damping should be removed from the data measured from a shortened tether on the ground when ultimately the damping properties of a full scale system in space are desired.

For a tethered satellite system, the damping ratio of all tether longitudinal structural vibration modes (excludes the mass-spring mode) are the same. They are determined by the tether's structural damping coefficient that is independent of tether length. The damping ratio of the mass-spring mode of the system depends on the tether length and the satellite mass. This damping ratio is less than that of the structural vibration modes by a factor of the square root of the tether/satellite mass ratio. For the 20 km TSS-1 tethered satellite system, the damping ratio of the mass-spring mode is expected to be approximately 5.5 %. Using the TSS-1 tether on a 2 km system with a 1000 kg satellite would result in a damping ratio of 1.2 %.

Lateral vibrations of tethered satellite systems are poorly damped because the damping arises from its non-linear coupling into the longitudinal mode. The equivalent damping ratio of lateral vibration modes are proportional to their squared amplitudes, which makes the damping ratio extremely low for small amplitude vibration. For a 20 km TSS-1 tether, it

takes 60 hours for the amplitude/length ratio to decay from 5 % to 1 % and a year to decay from 1 % to 0.1 %. For a 2 km TSS-1 tether, it takes 6 hours for the ratio to decay from 5 % to 1 % and a month from 1 % to 0.1 %.

The jump-rope mode is a special combination of lateral vibrations in two orthogonal planes. Since the tether length is not varying in the jump-rope mode, it has no damping. However, it will be precessed into an exchange mode between planar vibration and the jump-rope rotation because the natural frequencies are slightly different for the lateral vibration in and perpendicular to the orbit plane. The equivalent damping ratio for such a mode is about half of that for a planar lateral vibration mode.

Compared with the TSS-1 tether, higher damping material and better braided multi-layer structure may increase damping ratios of all vibration modes of a tethered satellite system. However, a substantial increase would be surprising. Practically, this increase would benefit mainly the longitudinal vibrations, which might be especially helpful for the mass-spring mode. For lateral vibrations, an increase in the damping ratio is desirable for a quiet system environment, which may be difficult to achieve by a passive means.

Some active damping device might be required for applications demanding high stability and low dynamic noise. Reeling the tether in and out at either end and moving the tether attachment point on the satellite are two of the options. For the case of an electrically conductive tether, the electrodynamic force may possibly be used to damp the lateral motion, although it may require large currents.

A more complete discussion of tether damping ideas is contained in [13].

3 Experimental Results of the Laboratory Simulator

3.1 Introduction

Typically, a major requirement of current space missions is the attitude control of the specific spacecraft. Whether the entire space vehicle, or simply a sub-system (e.g., a camera or antenna) is of interest, the angular orientation of the constellation must be regulated. In some instances, small angular tolerances are required in order to achieve the desired mission. In these cases, much effort must be concentrated in designing a control system to meet the required attitude specifications.

Recently, tethered satellite configurations have received much attention as new and potentially advantageous satellite constellations. Some proposed uses include the tethering of micro-gravity experiments, tethering electric power generators, tethering a remote docking port, and tethering instrument platforms from the proposed Space Station. In all of these proposed uses, the advantages of tethered configurations have been well documented by Becky [14]. The most obvious advantage is disturbance isolation from the parent spacecraft while maintaining a close working proximity. Implicit in this list of uses is the ability to regulate the attitude orientation of the tethered satellite.

A number of conventional methods currently exist to perform the attitude control of a tethered satellite. However, the tether tension force can generate such large disturbances that the control effort required to perform attitude control would be intolerably large. It has been shown by Lemke, Powell, and He [3] that, in practice, it is mandatory to vary the position of the tether attachment point with respect to the satellite mass center and to use this attach point motion to generate control torques. This is the basis of the design of the Kinetic Isolation Tether Experiment (KITE) and the laboratory simulator whose description follows. The simulator has been built as an effort to gain valuable experience in the design and construction of a tethered satellite control system which makes use of tether attach point motion to generate control torques. Also, it is desirable to investigate the

effects of tether and other non-linear dynamics on the performance of the proposed attitude control system and to exhibit theoretical angular stability performance in the laboratory and then extrapolate these findings to the flight test situation.

KITE is a proposed implementation of the attitude control method described above which will use an astrophysical pointing platform as a demonstration case on a future Space Shuttle mission [3]. This discussion considers a one dimensional simulation of the KITE flight experiment. An air bearing supported vehicle has been built and provisions have been made to tether the vehicle in a micro-gravity field and to vary the position of the attachment of the tether on the satellite. Digital control algorithms have been implemented which use attitude sensor information to position the tether attach point with respect to the vehicle mass center in such a way as to provide closed-loop attitude control.

3.2 Experimental Equipment

3.2.1 Simulator Hardware

A schematic diagram of the setup for the laboratory experiment is shown in Figure 8. This figure shows an air bearing supported vehicle on top of a very smooth granite table and a tether connecting the simulator to a nearby wall. The air bearing support rides on a thin gas film which is approximately .003 inches thick. This configuration provides the vehicle with three degrees of freedom (two linear, one rotational) on the table top, all of which exhibit extremely low friction. A schematic diagram of a side view of the experiment is shown in Figure 9. This figure shows that the granite table is tilted a small angle μ with respect to the horizontal. The table tilt results in a tether tension force which has the same character as that which is found in the orbital case. Currently, the table tilt angle has been adjusted such that $\mu \approx 2$ arc-minutes, which simulates the micro-gravity field experienced by a 2 km long tethered satellite. The gas in the cylinders on the vehicle is used to float the air bearing. The on-board electronics consist of a digital computer, a driver for the stepper motor, interfaces to the sensors, and batteries which provide power. The tether is attached to the positioning table on the simulator at one end, and to a wall

at the other end. The positioning table and the stepper motor are used to vary the position of the attachment point relative to the mass center of the entire vehicle, thereby providing the means of generating control moments for attitude control.

The simulator vehicle consists of two components: an air bearing flotation plate and a chassis plate. The flotation plate is a 1 inch thick, 40 inch diameter, circular aluminum disk. The underside of this plate is ground flat to approximately .001 inches, which provides a smooth surface for the vehicle to ride on. The center of the flotation plate is fitted with a small threaded hole which serves as a gas supply hook-up. The gas (dry nitrogen) passes through the plate, enters a 6 inch diameter plenum on the underside of the plate, and then flows out to the surrounding environment between the granite table and the air bearing.

The chassis plate is a 40 inch diameter disk made of .5 inch thick aluminum. The chassis is positioned on top of the flotation plate by means of two locating pins. The weight of the chassis is distributed on the air bearing with a .375 inch diameter solid o-ring positioned between the plates at two-thirds of the outer radius. This weight distribution scheme was chosen in order to minimize load variations from the chassis on the air bearing plate and to minimize the deflection of the air bearing due to the loading. A top view of the position of the components mounted on the chassis is shown in Figure 10. The individual components are arranged in a symmetric fashion about the center of the plate. This mounting style helps to ensure that the center of the plate will be the mass center of the entire vehicle. The computer card cage houses the on-board digital computer (8088 CPU), memory (static and dynamic RAM and EPROM), analog/digital converter, voltage transformers, and an interface to the stepper motor. The stepper motor card cage contains the indexer and driver electronics necessary to turn the stepper motor.

An important component of any closed-loop control system is the sensor configuration. Currently, the KITE attitude dynamics simulator contains a combination of two sensors: a coarse sensor with a large dynamic range and a relatively high noise level, and a fine sensor which has a limited dynamic range and a small noise level. The goals of the laboratory experiments to be performed with the simulator are to exhibit large angle slewing capability of ± 30 deg and to show fine pointing ability on the order of 1 arc-second.

Hence, the two sensors can be used in combination to provide the large angle sensing required for the slewing capability and to provide the accurate angle measurement required for the very accurate fine pointing.

A schematic of the coarse sensor is shown in Figure 11. This sensor is constructed of two phototransistors mounted 90 deg relative to each other. Phototransistors operate in the same fashion as bipolar transistors, with one exception. The phototransistor emitter current is proportional to the light energy incident upon the radiation sensitive collector-base junction, whereas the bipolar transistor emitter current is proportional to the base current. Therefore, the phototransistor current output is proportional to the product of the source intensity and the cosine of the incidence angle. The pair of phototransistors mounted as shown in Figure 11 and positioned as shown in the figure with respect to a distant light source can be used to measure the angle of the transistor mount relative to the light. This is accomplished by connecting the respective base-emitter junctions to ground through a series resistor. The voltage drop across these two identical resistors is then differenced and the result is a linear measure of the orientation of the transistor mount relative to the light source. The static output of this sensor is shown in Figure 12. The dynamic range of the sensor is shown to be ± 40 deg and the RMS noise level is approximately 76.7 arc-seconds.

The high accuracy angle sensor takes the form of an autocollimator. A schematic diagram of the optical hardware for an autocollimator is shown in Figure 13. This diagram shows a condenser lens which serves to collect and focus the light from the light source. This beam of collected light then bounces off the reflecting surface of a beam splitter and lands on the objective lens. The objective lens serves as a collimating lens for the light traveling away from the beam splitter. If the angle of the mirror, β, is zero, the collimated beam is reflected back upon itself and passes through the objective lens heading back through the beam splitter (in the non-reflecting direction) and is focused as a point on the optical axis. If the mirror angle β is finite, the collimated beam is reflected from the mirror in an off axis direction. The light then passes through the objective lens which focuses the beam at a distance, d, from the optical axis. The value of d is given by:

$$d = (2\beta)f,$$

where f is the objective lens focal length. Measuring d with a light sensitive

substrate provides a signal proportional to the angle of the mirror relative to the collimated beam. The autocollimator in use on the KITE simulator was developed by Lorell [15] for the work he did in the precision attitude control of spinning bodies. Figure 14 shows the static output of this autocollimator to possess an RMS noise level of 1.5 arc-seconds and a dynamic range of ± 1 deg.

The two previously described sensors are used in combination such that the advantages of each are used to the fullest. Ultimately, it is desirable to implement a system which will provide the capability to perform high accuracy, large angle, slew maneuvers. Figure 15 shows a block diagram of a design of such a system which makes use of the two current sensors. The attitude of the simulator will be measured by both sensors simultaneously and the output of each will be connected to a multi-channel A/D converter. The switch shown in Figure 15 will actually be a software switch. The digital control system will constantly check the size of the attitude measurement and as the value of the angle consistently stays below .3 deg, the control system will switch from using the coarse light sensor output to using the autocollimator measurement. The compensator will not change, only the source of the angle measurement will. As is currently the case, the compensator will be connected to the stepper motor driver which positions the tether attach point appropriately to regulate the rotational dynamics of the simulator.

3.2.2 Relationship Between Laboratory and Flight Test Experiments

The current configuration of the laboratory simulator possesses physical characteristics which differ from the current design of the flight test vehicle. For example, the mass and moments of inertia of the laboratory simulator are different from the expected flight test configuration. In order to quantify how the dynamic behavior of the laboratory simulator will differ from the flight vehicle, important scaling parameters have been derived. These parameters include the micro-gravity field, the inertia/tension ratio, and the tether length. Table 1 is a summary of the values of these scaling parameters for the current laboratory configuration and for the present flight test design.

quantity	on orbit	in lab
micro-gravity, $g'(m/s/s)$	$3Ln^2 = .0082$	$G\sin\mu = .008$
inertia/tension, $I/mg'(m\text{-}s^2)$	≈ 30	≈ 20
tether length, $L(m)$	≈ 2000	≈ 2

Table 1: KITE Scaling Parameters

The micro-gravity field for the flight test and laboratory simulation are given by the expressions shown in Table 1. The on orbit micro-gravity field is the well known gravity-gradient, which is dependent on the length of the tether, L, and the orbital rate, n. In the laboratory simulation, the micro-gravity field is simply the local gravitational constant, G, times the sine of the granite table tilt angle, μ. As a result, the micro-gravity field of the simulator can be made equal to the on orbit field by simply adjusting the granite table tilt to the proper angle such that the given expressions are equal. As is evident from Table 1, the current laboratory simulation is implemented such that the micro-gravity field is the same as the nominal orbital case.

The inertia/tension ratio is a measure of the speed of angular response for both the on orbit and the laboratory situations. This ratio is given by the moment of inertia (vehicle mass times the square of the radius of gyration) about the axis of rotation, I, divided by the tether tension (vehicle mass, m, times the micro-gravity acceleration). This ratio reduces to the square of the radius of gyration of the vehicle divided by the micro-gravity acceleration. Since the laboratory micro-gravity field has been made equal to the orbital case, it is clear that the inertia/tension ratio is a function of the respective radii of gyration for the laboratory and orbital cases. As a result, the angular response times will scale according to the ratio of radii of gyration for the vehicles under consideration. Substituting the appropriate values for inertias and masses of the vehicles, Table 1 shows that the response time of the current flight test configuration will be approximately 50% slower than the laboratory simulator response time. As a result, when drawing conclusions about the flight test vehicle based on the results of the laboratory experiments, the above time scaling must be kept in mind. It should be noted that if the laboratory micro-gravity acceleration were to be decreased by 33%, then the inertia/tension ratio would be equal in

both the laboratory and on orbit situations. In this case, the dynamic response characteristics of the laboratory simulator would be comparable to the actual on orbit response.

The last quantity of interest shown in Table 1 is the tether length. The nominal design length for the current flight test configuration is 2 km. Obviously, there are physical constraints which prohibit the implementation of this long a tether in a laboratory environment. Currently, a 2 m long tether is attached from the laboratory simulator to a laboratory wall. In order to make this length of tether less stiff (so that unacceptably large tension variations are not generated by very small attach point motions), a rubber band has been inserted between the tether and the attach point at the wall. The frequency of the mass-spring mode oscillation of the vehicle on the end of this tether/rubber band configuration is approximately .16 Hz. Hence, any effect that this mode may have on the attitude control system performance can be recognized and adjusted if necessary. Currently, a system at the wall attach point is being designed such that the dynamics of the 2 km long tether can be simulated. This will be accomplished using the analytic results of He and Powell [13] by moving the relative position of the wall attach point (along the two directions parallel to the granite table top) with respect to the vehicle attach point position. With this simulation ability, the effects of tether dynamics on the attitude control system can easily be assessed.

3.3 Experimental Results

The previously described laboratory simulator has been used to perform a preliminary investigation of the performance of the proposed attitude control system which makes use of tether attach point motion to generate control torques. Specifically, digital control algorithms have been derived which make use of orientation information provided by the sensors to calculate the required attach point position relative to the mass center, thereby implementing closed-loop attitude control. To date, all of the experiments have been performed in the regulator mode (i.e., zeroing of initial conditions). As a result, in all instances, after the control algorithm has been loaded into the on-board computer, the initial angular conditions are set (i.e., the initial angle is adjusted to a finite value and the initial angular

velocity is made zero), and then the control program is initiated. Data are stored in the on-board computer while the control system is operating. After the control program ends, the data are transferred to a desk top computer for data analysis and plotting.

3.3.1 Large Angle Slew Experiments

The first series of experiments using the KITE dynamics simulator were designed to study the large angle slewing capability of the vehicle and control system. The vehicle was given a relatively large (on the order of 10-20 deg) initial angular displacement and the control algorithm was initiated. In all of these experiments, the control algorithm consisted of lead compensation and the phototransistor angle sensor provided the orientation information. The lead compensator was designed using root locus and frequency response techniques. The location of the compensator zero was chosen in order to increase the closed-loop system bandwidth, while the compensator pole was chosen to attenuate sensor noise at higher frequencies. An integral term was added in an effort to reject constant disturbances of the simulator orientation (i.e., inaccurate knowledge of the vehicle mass center location, steady gas leaks from the on-board cylinders, room air currents). A typical time history of the vehicle attitude is shown in Figure 16. This figure shows that the initial angular displacement was reduced to a narrow band of values (RMS of .09 deg) about the 0 deg measure. The peak time of the dynamic response is approximately 12 seconds and the overshoot is approximately 6 percent. This corresponds to a closed-loop system bandwidth of approximately .05 Hz.

3.3.2 Fine Pointing Control Experiments

The next series of experiments were performed in order to exhibit the fine pointing ability of the vehicle and the control system. In all of these experiments, the autocollimator was used to obtain vehicle orientation information. Because of the small dynamic range of this sensor, the initial angular displacement was limited to less than 1 deg, and was typically chosen to be approximately .5 deg. A constant gain, full state feedback control algorithm was designed and an estimator was also derived to provide an

estimate of the full state for feedback purposes. In addition, the estimator serves as a 'smart' differentiator to provide velocity information, as well as a smoother of sensor noise. The constant feedback gains for both the full state compensator and the state estimator were calculated using a pole placement algorithm. The plant pole locations (including the appended integral state) were chosen such that the closed-loop system would exhibit acceptable dynamic response characteristics and such that the tether attach point would not saturate the absolute position limits. The estimator poles were chosen such that the state estimate would converge to the actual state five to ten times faster than the closed-loop plant dynamics. A typical time history of the closed-loop attitude response is shown in Figure 17 and a version with a smaller scale is shown in Figure 18. These figures show that the initial attitude was reduced to a narrow band (± 20 arc-seconds) in approximately 60 seconds. The peak time and maximum overshoot are approximately 6 seconds and 40 percent, respectively, which corresponds to a closed-loop system bandwidth of approximately .08 Hz. The RMS deviation from zero of the attitude measurement for the time between 100 and 400 seconds is 4.92 arc-seconds. These figures also show a low frequency (approximately .01 Hz) oscillation, with an amplitude greater than sensor noise, of the attitude. As it turns out, this frequency is exactly the calculated frequency of the pendular mode of the simulator in the microgravity field. It is anticipated that disturbances introduced by this motion will be eliminated when the system to move the attach point at the wall (see Section 3.2.2) is complete. With the ability to move the wall attach point in such a way as to keep the tether constantly aligned with the microgravity field, the pendular mode of the simulator will be eliminated, and, as a result, so will any effect this motion has on the attitude dynamics.

In an effort to determine the effect of the elimination of this oscillatory mode from the angular response, 100 seconds of data was chosen and a sine wave (amplitude, frequency, and phase) was fit to these data. The least squares fit sine wave was then subtracted from the raw data, which effectively served to eliminate the effects of the pendular mode from the measurement. The results of this mathematical process are shown in Figures 19 and 20. Figure 19 shows the raw data time slice (from 275 to 375 seconds) superimposed with the least squares fit sine wave to the same data. Figure 20 shows the results of subtracting the least squares fit sine wave

from the raw data. The RMS deviation from zero is 4.23 arc-seconds before the low frequency mode was extracted, and is reduced to 3.35 arc-seconds after the pendular mode was subtracted from the measurement. These results show that some, but not all, of the deviation from pure measurement noise is due to the pendular mode. Currently, work is being undertaken in order to determine the origin of the additional disturbance exhibited by the angular measurement. Once the origin of the disturbance is determined, provisions can be made in the control algorithm or in the design of the tethered constellation in order to eliminate the effect.

3.4 Laboratory Simulator Conclusions

The design and construction of the KITE dynamics laboratory simulator has been completed. Preliminary experiments with the simulator have shown that the concept of moving the tether attach point on the satellite to generate control torques is a feasible method of providing attitude control for tethered satellites. Digital control algorithms have been derived and implemented which use orientation information provided by attitude sensors to calculate the necessary tether attach point position relative to the vehicle mass center. Both large angle slew motions and fine pointing maneuvers have been performed by the simulator in the regulator mode (i.e., zeroing of initial angular displacements). Large angle slew experiments have shown that an initial angular displacement of 12.5 deg can be reduced to an RMS value of .09 deg in approximately 15 seconds and that the closed-loop dynamic system possesses a bandwidth of approximately .05 Hz. Tests of the fine pointing ability of the simulator have shown that an initial angular displacement of 1500 arc-seconds can be reduced to an RMS value of 5 arc-seconds in less than 100 seconds, with a closed-loop bandwidth of .08 Hz.

Future work with the KITE dynamics laboratory simulator will center on the implementation of wall attach point motion. The ability to move the wall attach point with respect to the vehicle attach point and the vehicle center of mass will provide the ability to simulate both longitudinal and lateral tether dynamics. With this capability, the effects of these nonlinear dynamics on the performance of the control algorithm can easily be assessed. In addition, wall attach point motion will allow the elimination

of the pendular mode of the vehicle in the laboratory micro-gravity field. Also, with the ability to keep the tether parallel to the micro-gravity field, it is speculated that fine pointing accuracies of 1.5 arc-seconds (i.e., sensor noise limited) should be achievable in the laboratory. Work will also be undertaken to combine the two sensors in one experiment; a large angle slew followed directly by a fine pointing maneuver. This will demonstrate the ability of the vehicle and control concept to perform large angular motions with very high accuracies. Finally, studies will be undertaken to observe the effects of varying the scaling parameters previously discussed. For example, in order to reproduce the same time response characteristics in the laboratory as are expected on the flight test, experiments will be performed such that the laboratory inertia/tension ratio will take on the same value as the flight test ratio.

A more detailed discussion of the KITE laboratory simulator and the experimental work recently completed with it are available in [16].

References

[1] Lee Marshall : Martin Marietta internal memorandum TSS-86-LM-376, August 1986, private communication.

[2] W. A. Baracat and C. L. Butner : *Tethers in Space Handbook*, Prepared for NASA Office of Space Flight Advanced Programs, August 1986, Bantam Books, Inc.

[3] Larry Lemke, J. David Powell and Xiaohua He : "Attitude Control of Tethered Spacecraft," Presented in *NASA/AIAA/PSN International Conference on Tethers in Space,* 17-19 September 1986. Arlington, Virginia. AAS 86-211.

[4] David D. Lang, and Roger K. Nolting : "Operations with Tethered Space Vehicles," *Gemini Summary Conference,* February 1-2, 1967, Houston, Texas. NASA SP-138.

[5] Marshall H. Kaplan : *Modern Spacecraft Dynamics and Control,* John Willey and Sons, 1976.

[6] Leonard Meirovitch : *Analytical Methods in Vibrations*, The Macmillan Company, London, 1967.

[7] F. Graziani, S. Sgubini and A. Agneni : "Disturbance Propagation in Orbiting Tethers," Presented in NASA/AIAA/PSN International Conference on Tethers in Space, 17-19 September 1986, Arlington, Virginia.

[8] S. Bergamaschi and S. Cusinato : "Continuous Model for Tether Elastic Vibration in TSS," Presented in *AIAA 24th Aerospace Sciences Meeting*, January 1986, Reno, Nevada.

[9] Ruth Zucker: "Elementary Transcendental Functions Logarithmic, Exponential, Circular and Hyperbolic Functions," *Handbook of Mathematical Functions*, Edited by Milton Abramowitz, and Irene A. Stegun, Dover, New York, 1964, pp.75.

[10] Dominique Suchet : "Lateral Dynamics of A Tether," A report at Department of Aeronautics and Astronautics, Stanford University, June, 1986.

[11] E. Scala, and D. P. Bentley : "Design and Fabrication of the 20 KM / 10 KV Electromechanical Tether for TSS-1 Using High Impact Conductor (Hiwire)^{TM}," Presented in *NASA/AIAA/PSN International Conference on Tether in Space*, 17-19 September 1986, Arlington, Virginia.

[12] Donald L. Edberg, "Measurement of Material Damping in a Simulated Space Environment," Ph.D. dissertation, Dept. of Aeronautics and Astronautics, Stanford University, December 1984.

[13] Xiaohua He and J. David Powell, "Tether Damping in Space", presented at the Second International Conference on Tethers in Space, Venice, Italy, October 1987.

[14] Ivan Becky: "Space Station Enhancement Using Tethers," Presented at the International Astronautical Federation International Astronautical Congress, 35th, Lausanne, Switzerland, Oct. 7-13, 1984.

[15] Kenneth Lorell: "Precision Attitude Control of Symmetric Spinning Bodies," Ph.D. Dissertation, Stanford University, Stanford, California, April 1971.

[16] Robert Kline-Schoder and J. David Powell, "Recent Results of the KITE Attitude Dynamics Simulator", presented at the Second International Conference on Tethers in Space, Venice, Italy, October 1987.

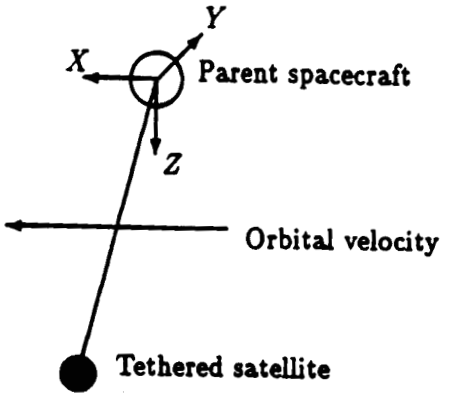

Figure 1: Orbiting coordinate system used

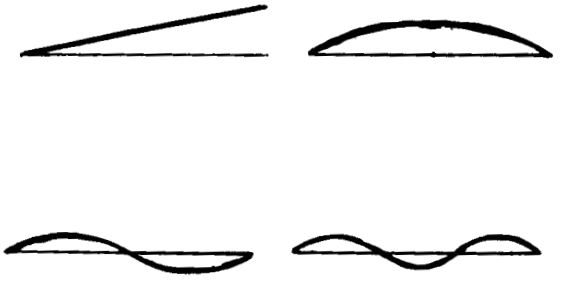

Figure 2: Lontitudinal mode shapes

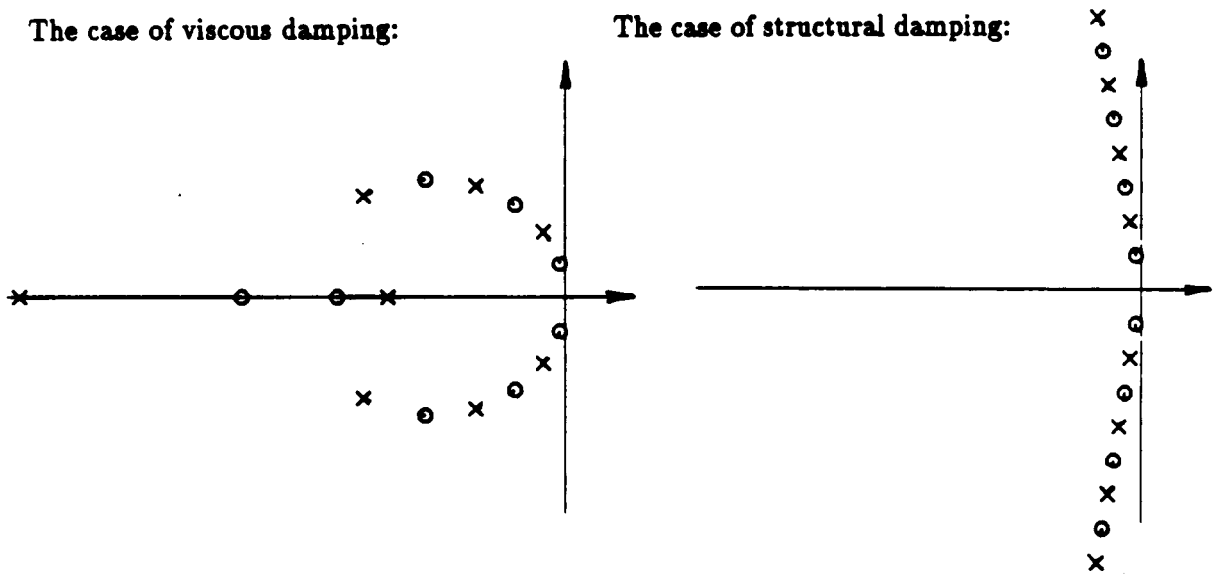

Figure 3: Pole-Zero locations of tether transfer function

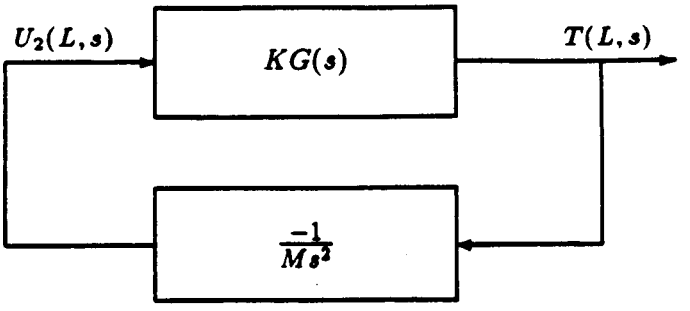

Figure 4: Block Diagram of Longitudinal System

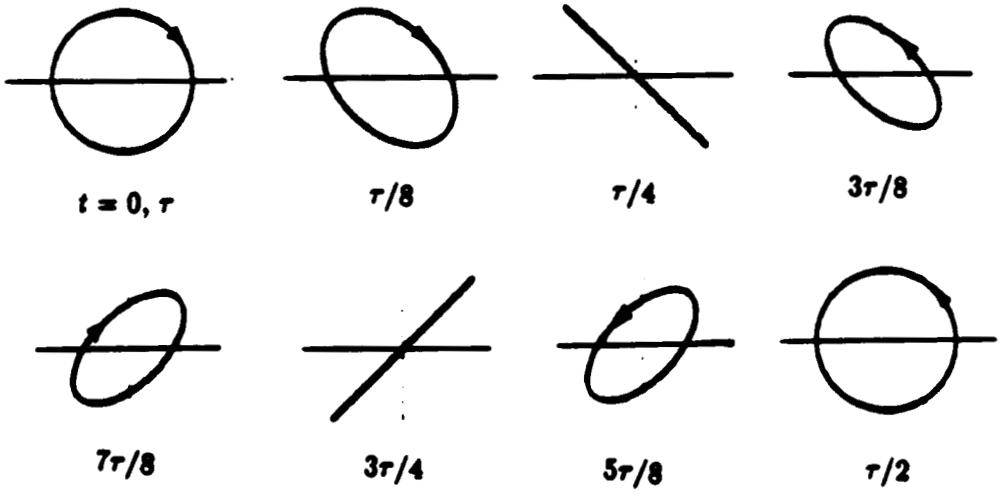

Figure 5: End view of jump-rope beat mode shapes at various times

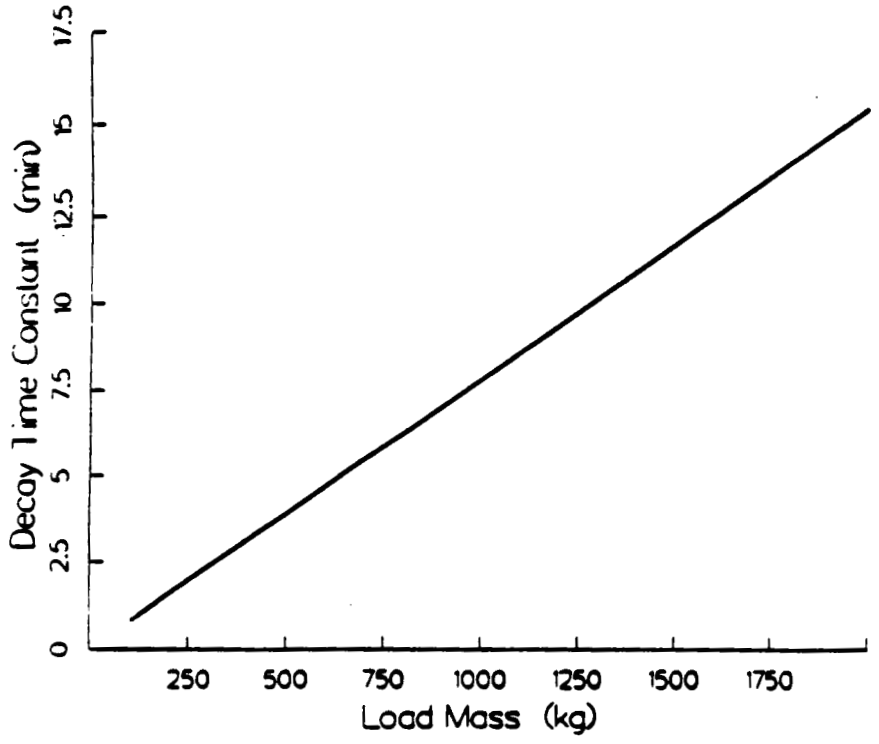

Figure 6: Damping time constant of mass-spring oscillation mode

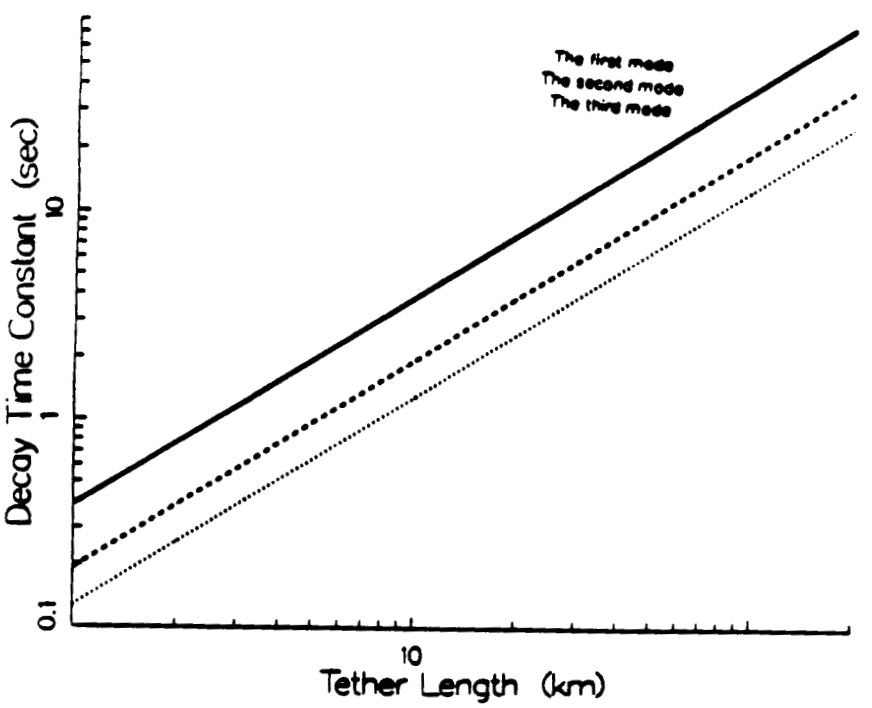

Figure 7: Damping time constant of structural vibration modes

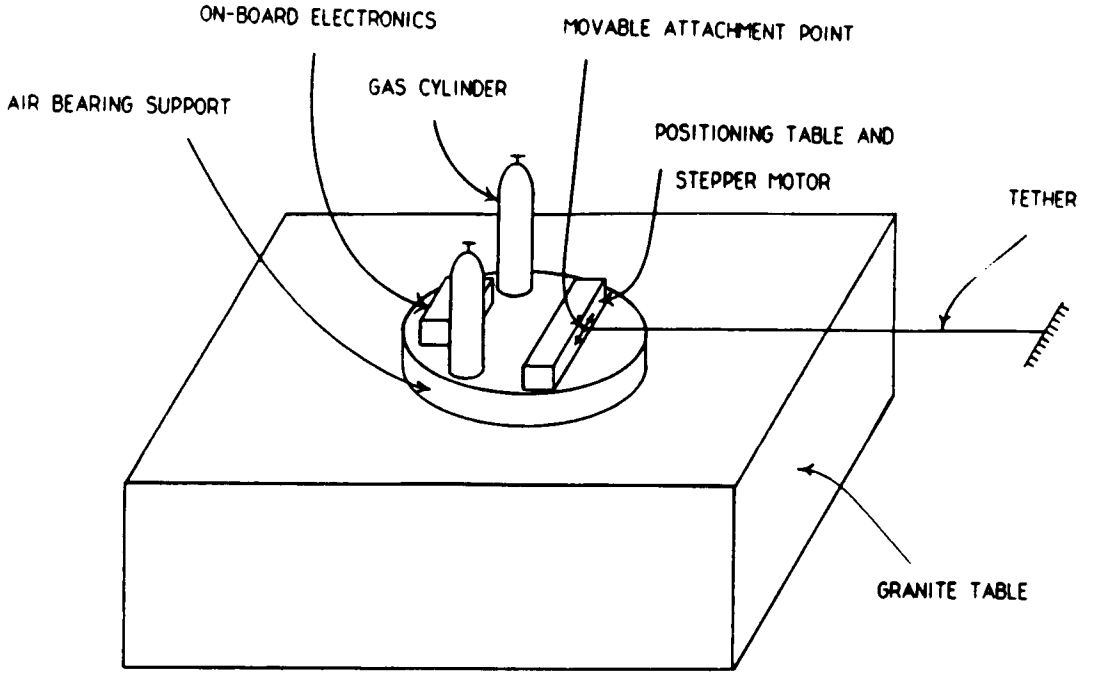

Figure 8: Schematic of Experimental Setup

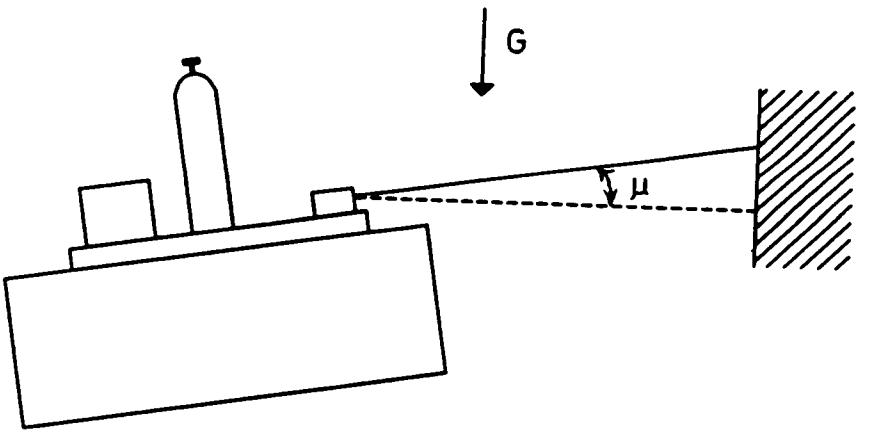

Figure 9: Schematic Side View of Experimental Setup

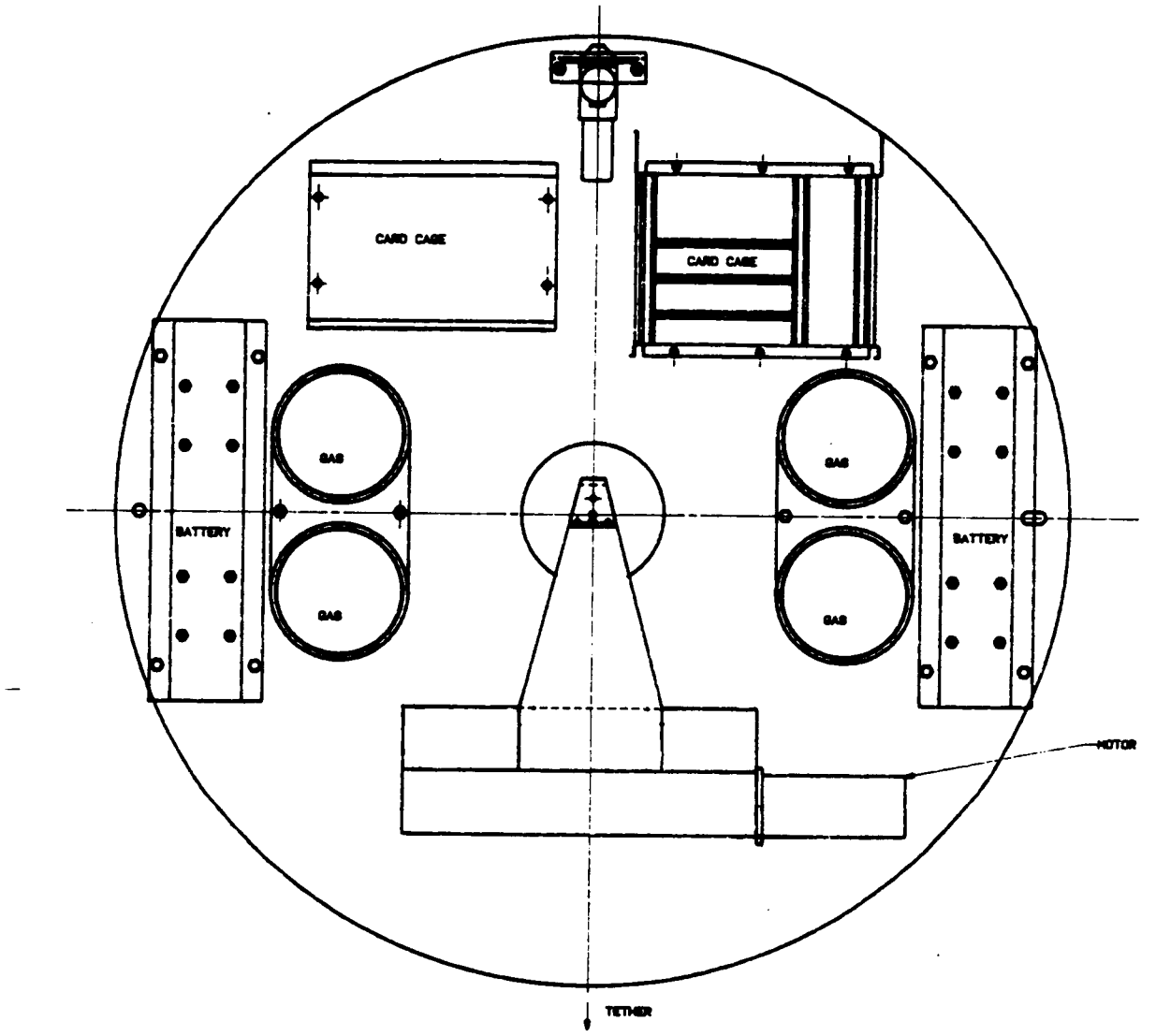

Figure 10: Component Layout of Chassis

Figure 11: Schematic of Coarse Phototransistor Angle Sensor

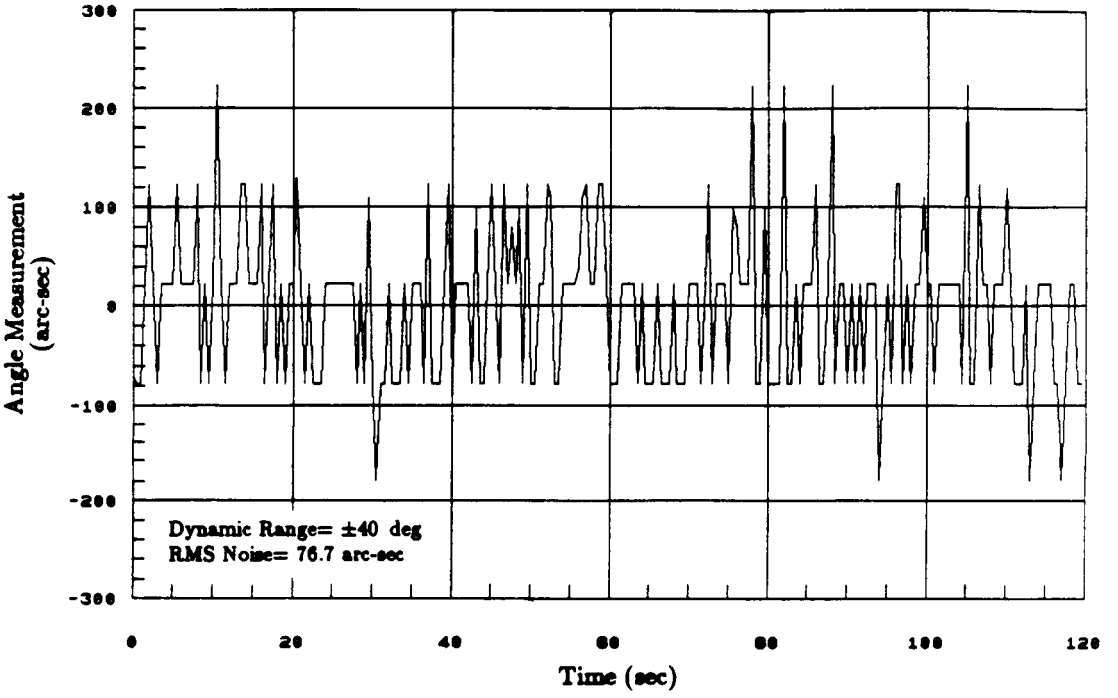

Figure 12: Static Coarse Angle Sensor Output

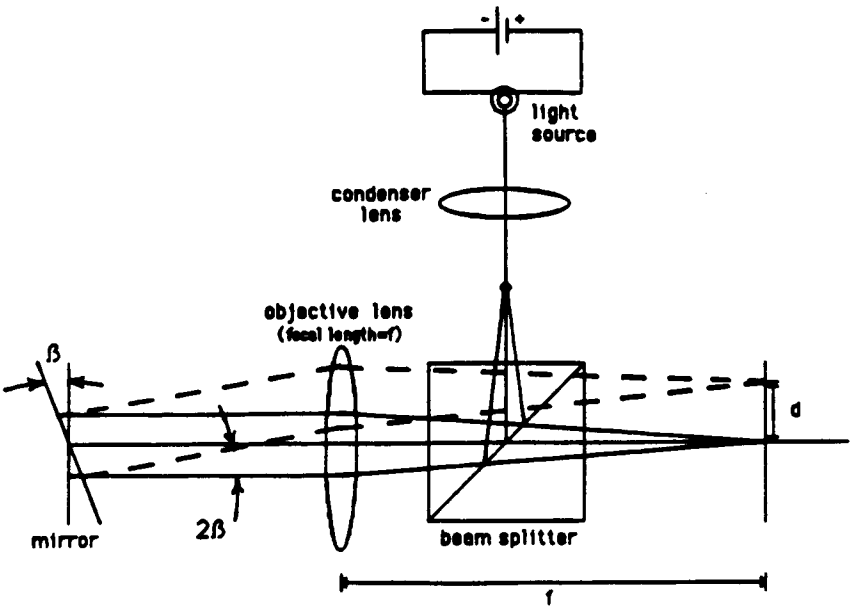

$d=(2ß)f$

Figure 13: Schematic of Autocollimator

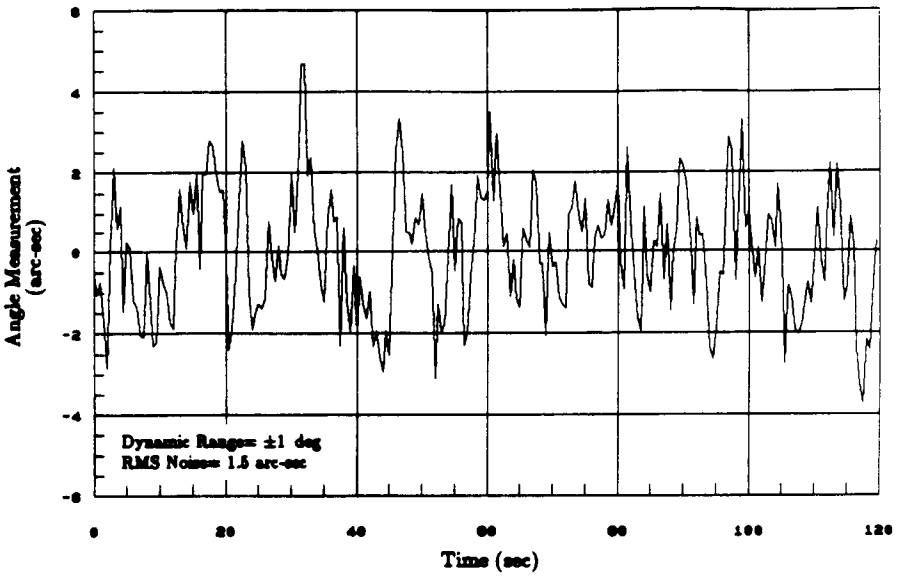

Figure 14: Static Autocollimator Output

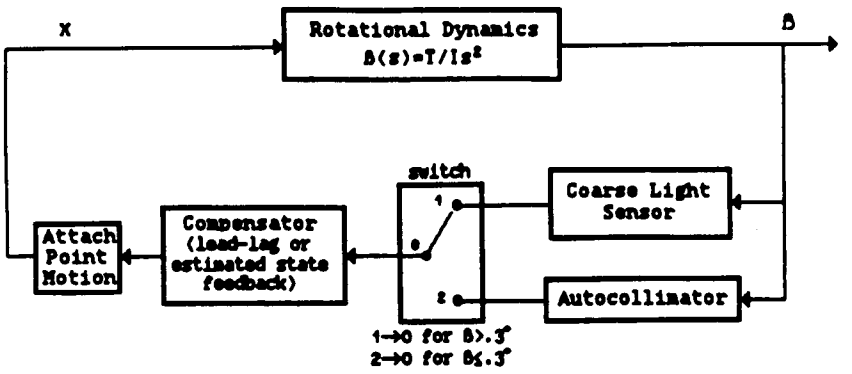

Figure 15: Control Law and Sensor Switching Block Diagram

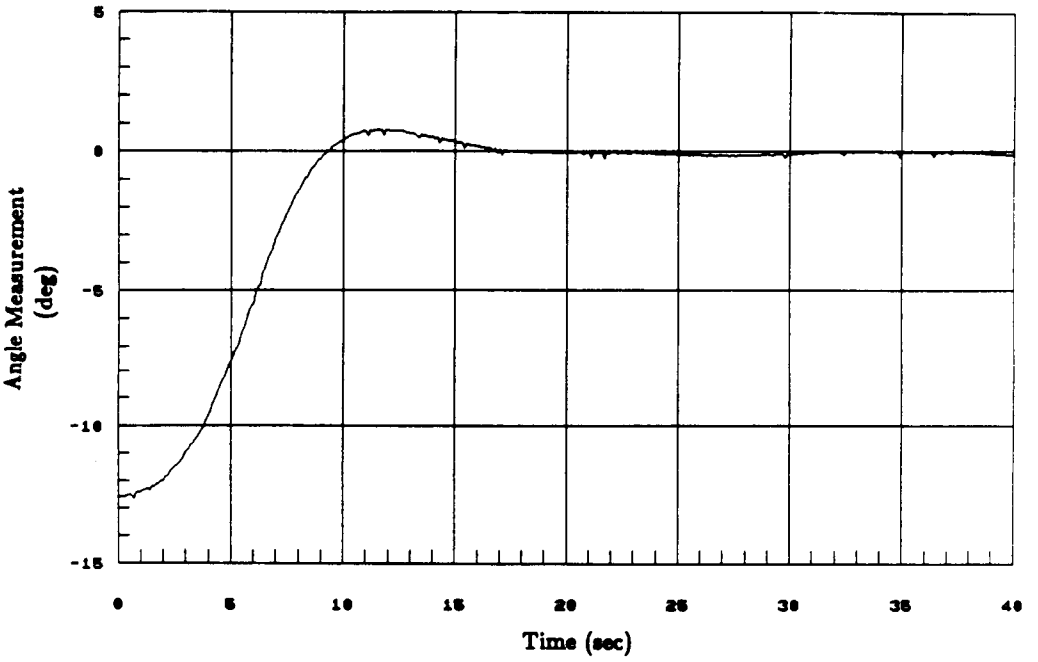

Figure 16: Large Angle Slew Maneuver

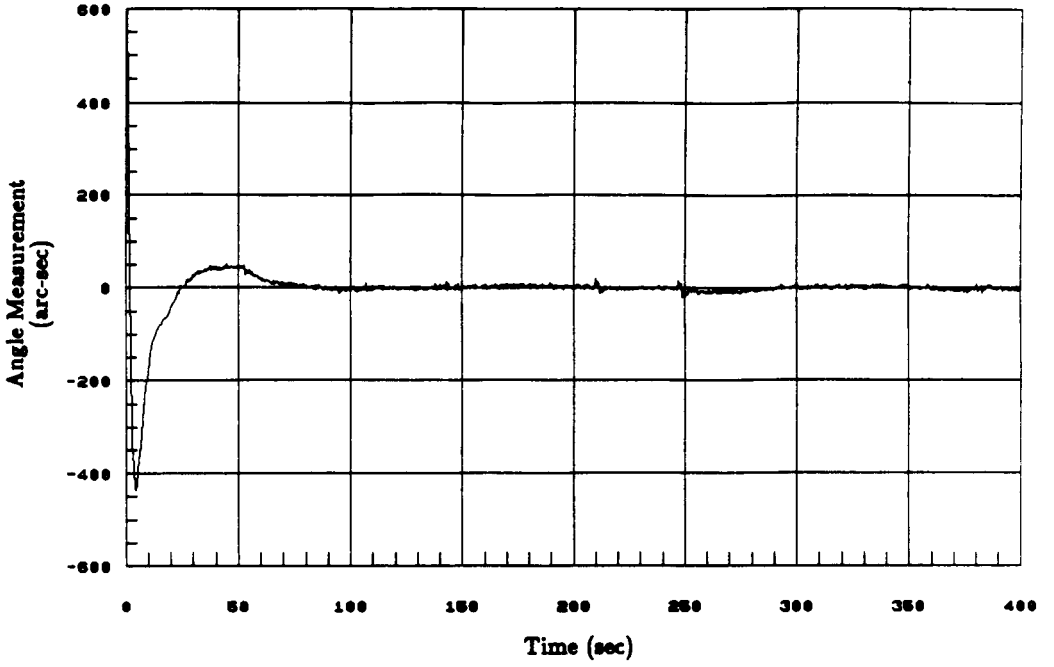

Figure 17: Fine Pointing Time History

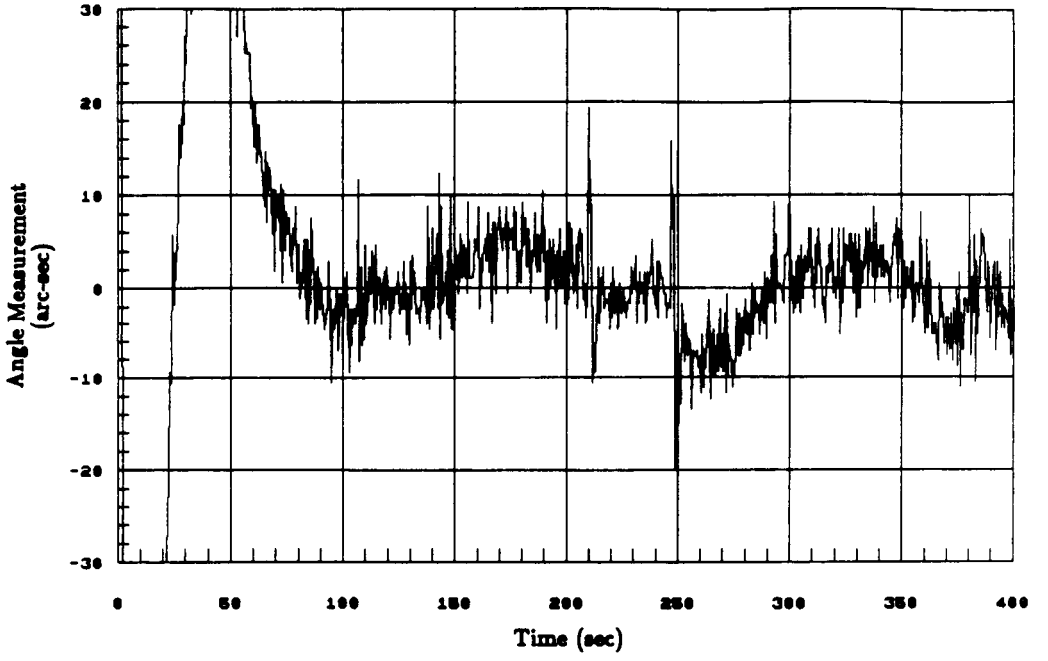

Figure 18: Fine Pointing Time History

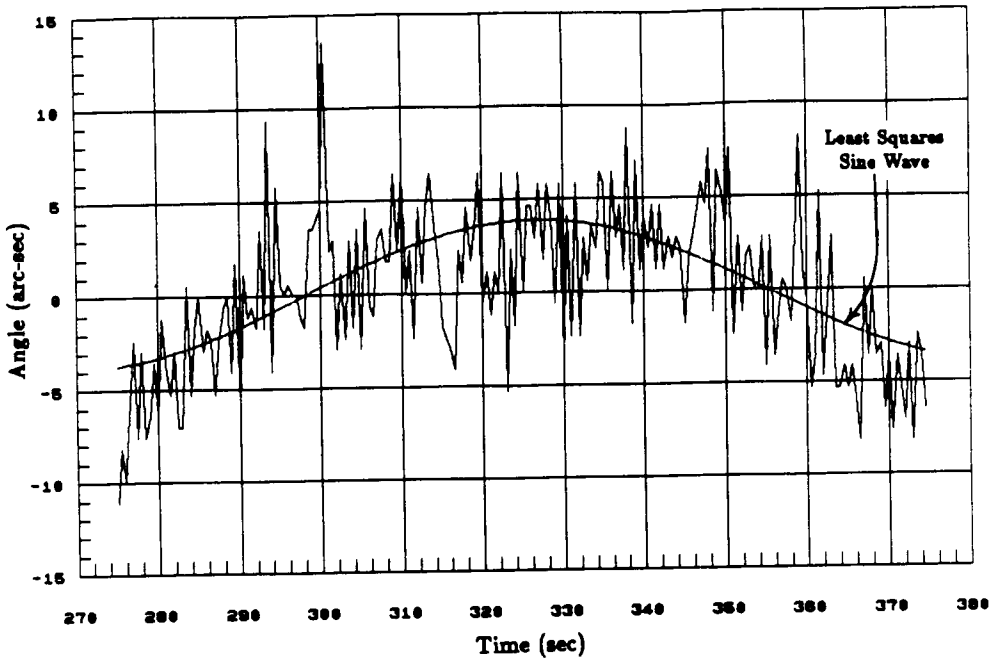

Figure 19: Measured Angle and Least Squares Fit Sine Wave

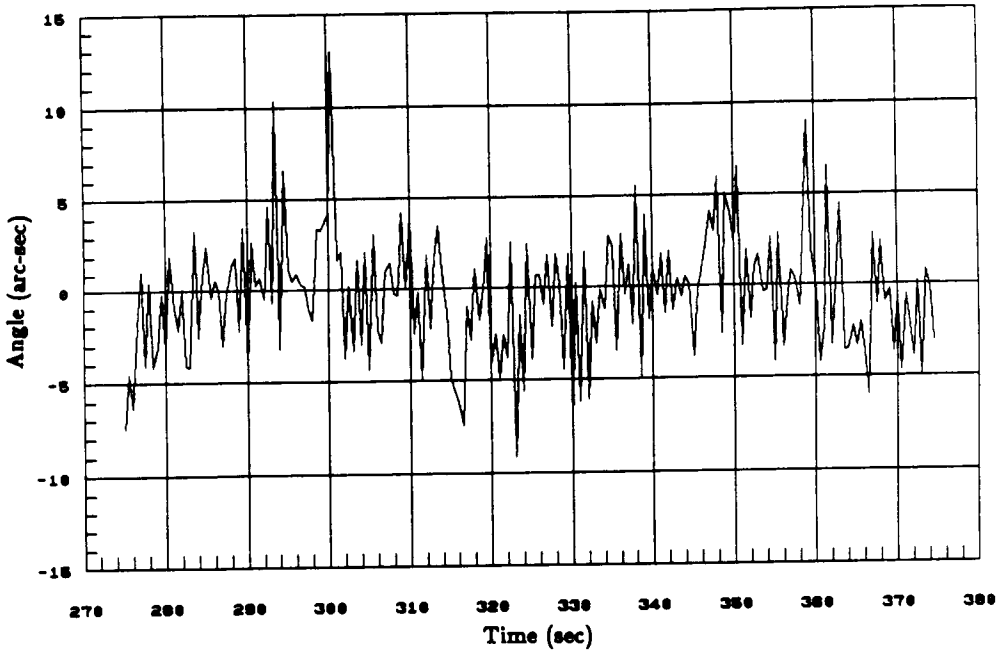

Figure 20: Measured Angle Minus Least Squares Fit Sine Wave